



Three-Dimensional Simulations of Liquid Feed Direct Methanol Fuel Cells

Wenpeng Liu^{*,a} and Chao-Yang Wang^{*,z}

Electrochemical Engine Center and Department of Mechanical and Nuclear Engineering,
The Pennsylvania State University, University Park, Pennsylvania 16802, USA

Recent research indicates that performance and design of a liquid feed direct methanol fuel cell (DMFC) is controlled not only by electrochemical kinetics and methanol crossover but also by water transport and by their complex interactions in the design regime for portable electronics applications. In this paper, a three-dimensional (3D), two-phase model is presented for DMFCs, in particular considering water transport and treating the catalyst layer explicitly as a component rather than an interface without thickness. Other features of the model are similar to an earlier version published in 2003. The DMFC model is based on the multiphase mixture formulation and encompasses all components in a DMFC using a single computational domain. A flow solver, Fluent, is employed to simultaneously solve flow, species, and charge-transport equations. Numerical simulations in 3D are carried out to explore mass transport phenomena occurring in DMFCs for portable applications as well as to reveal an interplay between the local current density and methanol crossover rate. Numerical results also indicate that the anode flow field design and methanol feeding concentration are two key parameters for optimal cell performance.

© 2007 The Electrochemical Society. [DOI: 10.1149/1.2429041] All rights reserved.

Manuscript submitted August 15, 2006; revised manuscript received October 30, 2006. Available electronically February 2, 2007.

The direct methanol fuel cell (DMFC) is considered a leading contender for next-generation portable and micropower sources, offering a combination of simplicity, robustness, and high energy density due to the use of liquid methanol. The basic principles of a DMFC can be found in the literature¹ and thus are not repeated here.

In order to compete with lithium-ion batteries, a portable DMFC system must overcome several key technical challenges: (i) low rate of methanol oxidation kinetics, (ii) methanol crossover through the polymer membrane, (iii) water crossover from the anode to cathode,^{2,3} and (iv) thermal management. While new materials are being pursued to solve these problems, innovative designs can also be developed with the materials presently available. As a result, there is an urgent need for understanding, prediction, and optimization of various interactive transport and electrochemical processes that occur in portable DMFCs.

Much DMFC research in the past has focused upon the first two issues, methanol oxidation kinetics and methanol crossover, by studying electrocatalysis and electrolyte membrane materials.⁴⁻¹⁴ The more recent interest in small-scale DMFC systems for application to portable and micropower^{15,16} entails a unique design regime under lower temperatures and ambient pressure as well as a better understanding of methanol, water, and heat transport. For this purpose, visualization of two-phase flow in the DMFC anode was carried out by Argyropoulos et al.,¹⁷ and Lu and Wang.¹⁸ Nonetheless, no work has attempted to quantitatively describe two-phase flow phenomena in a DMFC.

In tandem with experimental efforts, mathematical modeling of DMFCs has received much attention with the goal of having a design tool to design and optimize cell structures under a myriad of operating conditions and form factors. Focusing on either one or two dimensions, early DMFC modeling works were developed to study the mass transport phenomena, electrochemical processes, and their interactions.¹⁹⁻²⁴ However, the two-phase effects, recently found to be of paramount importance to understand DMFC behaviors, were not considered in these earlier models. In a three-part paper,²⁵⁻²⁷ Meyers and Newman developed a theoretical framework that describes the equilibrium of multicomponent species in the membrane. The transport of species in the membrane based on concentrated-solution theory and membrane swelling was taken into account. The transport phenomena in the porous electrode were also included.

However, the effects of flow and stoichiometry were not considered. In addition, carbon dioxide was assumed to be dilute enough to remain fully dissolved in liquid.

Wang et al.²⁸ successfully applied the multiphase mixture (M^2) modeling framework of Wang and Cheng²⁹ to simulate two-phase flow and transport in the air cathode of a polymer electrolyte fuel cell. They suggested that capillary action is the dominant mechanism for liquid water transport through the gas diffusion layer (GDL). Later, this model was extended for a DMFC by Wang and Wang³⁰ and simulation results showed the importance of the gas-phase transport of methanol in the two-phase anode GDL. A more thorough review of DMFC modeling was recently given by Wang.¹

Water transport, in addition to methanol and oxygen transport, has emerged as an important modeling issue for portable DMFCs where water budget must be considered in order to attain high energy density. Water transport has not been considered in all prior DMFC models and is addressed in this paper within the framework of three-dimensional (3D) numerical simulations. In addition, the present model, built upon an earlier model of Wang and Wang,³⁰ implements a full model for the catalyst layer instead of treating it as an interface.

In the following, a 3D, two-phase mathematical model of DMFCs with the above-mentioned features is presented. A commercial flow solver, Fluent, is then employed to solve two-phase flow, species, and charge-transport equations simultaneously. Model results are presented to illustrate the intricate interplay between the local current density and methanol crossover rate distributions, and to pinpoint key parameters for the cell design and optimization.

Model

The present 3D model was extended from that of Wang and Wang³⁰ and based on the M^2 formulation of Wang and Cheng,²⁹ which is particularly suitable and popular for two-phase fuel cell modeling. The specific assumptions made in this model include: (i) incompressible gas mixture, (ii) laminar flow due to a Reynolds number of the order of several hundreds, (iii) isothermal cells, (iv) isotropic and homogeneous porous GDL, characterized by an effective porosity and permeability, (v) negligible potential drop due to ohmic resistance in the electronically conductive solid matrix of GDL and catalyst layers, as well as bipolar plates. Furthermore, a homogeneous flow was assumed for the two-phase flow through channels of both anode and cathode. Therefore, the gas and liquid phase velocities were equal in the flow channels, resulting in a very small fraction of either CO₂ gas in the liquid stream of the anode channel (i.e., bubbly flow) or liquid water in the gas stream of the cathode channel (i.e., mist flow).

* Electrochemical Society Active Member.

^a Present address: MTI MicroFuel Cells Inc., Albany, NY 12205, USA.

^z E-mail: cwx31@psu.edu

Table I. Summary of governing equations in the 3D model.

Mass conservation equation

$$\partial(\varepsilon\rho)/\partial t + \nabla(\rho\mathbf{u}) = \dot{m}$$

where

$$\dot{m} = \begin{cases} M^{\text{MeOH}}S^{\text{MeOH}} + M^{\text{H}_2\text{O}}S^{\text{H}_2\text{O}} + M^{\text{CO}_2}j/(6F) & \text{anode catalyst layer} \\ M^{\text{H}_2\text{O}}S^{\text{H}_2\text{O}} + M^{\text{O}_2}S^{\text{O}_2} + M^{\text{CO}_2}j_{\text{xover}}/(6F) & \text{cathode catalyst layer} \end{cases}$$

Momentum conservation equation

$$1/\varepsilon[\partial(\rho\mathbf{u})/\partial t + 1/\varepsilon\nabla \cdot (\rho\mathbf{u}\mathbf{u})] = -\nabla p + \nabla \cdot \boldsymbol{\tau} + S_{\mathbf{u}}$$

where

$$S_{\mathbf{u}} = \begin{cases} 0 & \text{channels} \\ -\mu/K\mathbf{u} & \text{backing and catalyst layers} \end{cases} \text{ and } \mathbf{u} = 0 \text{ membrane}$$

MeOH transport equation

$$\partial/c_i^{\text{MeOH}}/\partial t + \nabla \cdot \{\gamma\mathbf{u}c_i^{\text{MeOH}}[s + (1-s)/k_H]\} = \nabla \cdot [D_{l,\text{eff}}^{\text{MeOH}} + D_{g,\text{eff}}^{\text{MeOH}}/k_H]\nabla c_i^{\text{MeOH}} - \nabla \cdot \{[1/\rho_l - 1/(k_H\rho_g)]c_i^{\text{MeOH}}\mathbf{j}_l\} + S^{\text{MeOH}}$$

where

$$S^{\text{MeOH}} = -(j + j_{\text{xover}})/(6F) \quad \text{anode catalyst layer}$$

Water transport equation

$$\partial c_i^{\text{H}_2\text{O}}/\partial t + \nabla \cdot \{\gamma\mathbf{u}c_i^{\text{H}_2\text{O}}\} = \nabla \cdot [D_{l,\text{eff}}^{\text{H}_2\text{O}}\nabla c_i^{\text{H}_2\text{O}}] - \nabla \cdot [(c_i^{\text{H}_2\text{O}}/\rho_l - c_{g,\text{sat}}^{\text{H}_2\text{O}}/\rho_g)\mathbf{j}_l] + S^{\text{H}_2\text{O}}$$

where

$$S^{\text{H}_2\text{O}} = \begin{cases} -j(1 + 6\alpha)/(6F) & \text{anode catalyst layer} \\ j/(2F) + j_{\text{xover}}/(3F) + \alpha j/F & \text{cathode catalyst layer} \end{cases}$$

Oxygen transport equation

$$\partial c_i^{\text{O}_2}/\partial t + \nabla \cdot \{\gamma\mathbf{u}c_i^{\text{O}_2}\} = \nabla \cdot [D_{g,\text{eff}}^{\text{O}_2}\nabla c_i^{\text{O}_2}] - \nabla \cdot [(c_i^{\text{O}_2}/\rho_g)\mathbf{j}_l] + S^{\text{O}_2}$$

where

$$S^{\text{O}_2} = -(j + j_{\text{xover}})/(4F) \quad \text{cathode catalyst layer}$$

Proton transport equation

$$0 = \nabla \cdot (\kappa_{\text{eff}}\nabla\Phi_e) + S_{\Phi}$$

where

$$S_{\Phi} = \begin{cases} j & \text{anode catalyst layer} \\ -j_c + j_{\text{xover}} & \text{cathode catalyst layer} \end{cases}$$

Electrochemical kinetics

$$j = a_{o,a}^{\text{ref}}c_l^{\text{MeOH}}|_{\text{cata}}\exp[(\alpha_a F\eta_a)/(RT)]/c_l^{\text{MeOH}}|_{\text{cata}} + K_c\exp[(\alpha_c F\eta_c)/(RT)]$$

where

$$\eta_a = \Phi_s - \Phi_e - U_a^o \text{ (with } \Phi_s = 0 \text{ in the anode)}$$

and

$$j_c = a_{o,c}^{\text{ref}}(c_g^{\text{O}_2}|_{\text{cata}}/c_g^{\text{O}_2,\text{ref}})(1-s)\exp[-(\alpha_c F\eta_c)/(RT)]$$

where

$$\eta_c = \Phi_s - \Phi_e - U_c^o \text{ (with } \Phi_s = V_{\text{cell}} \text{ in the cathode)}$$

Mass conservation.— A generic mass conservation equation, valid for all components including channels, backing layers, catalyst layers of both anode and cathode, and the membrane, can be written as

$$\frac{\partial(\varepsilon\rho)}{\partial t} + \nabla \cdot (\rho\mathbf{u}) = \dot{m} \quad [1]$$

where

$$\dot{m} = \begin{cases} M^{\text{MeOH}}S^{\text{MeOH}} + M^{\text{H}_2\text{O}}S^{\text{H}_2\text{O}} + M^{\text{CO}_2}\frac{j}{6F} & \text{anode catalyst layer} \\ M^{\text{H}_2\text{O}}S^{\text{H}_2\text{O}} + M^{\text{O}_2}S^{\text{O}_2} + M^{\text{CO}_2}\frac{j_{\text{xover}}}{6F} & \text{cathode catalyst layer} \end{cases} \quad [2]$$

Detailed expressions for various species sources or sinks, S^k , are provided in Table I. Due to the species consumption and production

inside a DMFC, we have different mass source-sink terms, \dot{m} , applied in the anode and cathode catalyst layers, respectively. In the anode catalyst layer, the mass source is caused by methanol consumption and crossover through the membrane, water consumption and crossover through the membrane, and carbon dioxide generation by the anodic reaction. In the cathode catalyst layer, the mass source term includes water generation and flux from the anode, oxygen consumption by the cathodic reaction, and carbon dioxide generation due to the parasitic oxidation reaction of crossover methanol.

Momentum equation.— The momentum equation can be given by

$$\frac{1}{\varepsilon}\left[\frac{\partial(\rho\mathbf{u})}{\partial t} + \frac{1}{\varepsilon}\nabla \cdot (\rho\mathbf{u}\mathbf{u})\right] = -\nabla p + \nabla \cdot \boldsymbol{\tau} + S_{\mathbf{u}} \quad [3]$$

where

$$S_{\mathbf{u}} = \begin{cases} 0 & \text{channels} \\ -\frac{\mu}{K}\mathbf{u} & \text{backing and catalyst layers} \end{cases} \quad [4]$$

and

$$\mathbf{u} = 0 \quad \text{membrane} \quad [5]$$

Here, the fluid velocity in the backing and catalyst layers is described by Darcy's law and applied for single- and two-phase flow, while in the membrane it is assumed to be zero due to the negligible convective velocity through nanopores of the membrane.

General species transport equation.—The general conservation equation for a species can be written, in the form of mass fraction, as³⁰

$$\frac{\partial}{\partial t}(\rho Y^k) + \nabla \cdot (\gamma \rho \mathbf{u} Y^k) = \nabla \cdot [\rho_l D_{l,\text{eff}}^k \nabla Y_l^k + \rho_g D_{g,\text{eff}}^k \nabla Y_g^k] - \nabla \cdot [(Y_l^k - Y_g^k) \mathbf{j}_l] + \dot{m}^k \quad [6]$$

where Y^k stands for the mixture mass fraction of methanol, water, and oxygen in the two-phase mixture. Note that the advection correction factor, γ , is equal to unity in the channel regions due to the homogeneous flow assumption made earlier, but nonunity in backing and catalyst layers because the M^2 model for a porous medium is a two-fluid model. In addition, the effective diffusion coefficients in the liquid and gas phases are given, respectively, by

$$D_{l,\text{eff}}^k = (\varepsilon s)^{1.5} D_l^k \quad \text{and} \quad D_{g,\text{eff}}^k = [\varepsilon(1-s)]^{1.5} D_g^k \quad [7]$$

Based on the relation between species mass fraction and molar concentration

$$\rho Y^k = c^k M^k \quad [8]$$

and the two-phase property definition²⁹

$$\rho Y^k = \rho_l Y_l^k s + \rho_g Y_g^k (1-s) \quad [9]$$

we have the following species equation in terms of molar concentration

$$\begin{aligned} & \frac{\partial}{\partial t} [c_l^k s + c_g^k (1-s)] + \nabla \cdot \{ \gamma \mathbf{u} [c_l^k s + c_g^k (1-s)] \} \\ & = \nabla \cdot [D_{l,\text{eff}}^k \nabla c_l^k + D_{g,\text{eff}}^k \nabla c_g^k] - \nabla \cdot \left[\left(\frac{c_l^k}{\rho_l} - \frac{c_g^k}{\rho_g} \right) \mathbf{j}_l \right] + S^k \end{aligned} \quad [10]$$

In the above, constant liquid and gas densities, ρ_l and ρ_g , have been assumed.

Defining the mixture molar concentration, c^k , as

$$c^k = c_l^k s + c_g^k (1-s) \quad [11]$$

the species equation, Eq. 6, can be rewritten as

$$\begin{aligned} & \frac{\partial c^k}{\partial t} + \nabla \cdot \{ \gamma \mathbf{u} c^k \} = \nabla \cdot [D_{l,\text{eff}}^k \nabla c_l^k + D_{g,\text{eff}}^k \nabla c_g^k] \\ & - \nabla \cdot \left[\left(\frac{c_l^k}{\rho_l} - \frac{c_g^k}{\rho_g} \right) \mathbf{j}_l \right] + S^k \end{aligned} \quad [12]$$

where c_l^k and c_g^k stand for species molar concentrations in the liquid and gas phases, respectively.

The second term on the right side of Eq. 12 represents species transfer caused by relative motion of liquid to gas phase under capillary action in the porous backing and catalyst layers. In this term, the capillary-diffusional flux of the liquid phase, \mathbf{j}_l , as defined in Eq. 13, is directly proportional to the gradient in capillary pressure, p_c , and thus, is related to the surface wetting characteristics of the porous materials. That is²⁹

Table II. Two-phase relations (Ref. 29).

Density	$\rho = \rho_l s + \rho_g (1-s)$
Molar concentration	$c = c_l s + c_g (1-s)$
Velocity	$\rho \mathbf{u} = \rho_l \mathbf{u}_l + \rho_g \mathbf{u}_g$
Kinetic density	$\rho_k = \rho_l \lambda_l(s) + \rho_g \lambda_g(s)$
Viscosity	$\mu = [\rho_l s + \rho_g (1-s)] [(k_{rl}/v_l) + (k_{rg}/v_g)]$
Diffusivity	$\rho D^k = \rho_l s D_l^k + \rho_g (1-s) D_g^k$
Advection correction factor	$\gamma = \rho (\lambda_l c_l^k / \rho_l + \lambda_g c_g^k / \rho_g) / c$
Relative mobility	$\lambda_l(s) = (k_{rl}/v_l) / [(k_{rl}/v_l) + (k_{rg}/v_g)]; \lambda_g(s) = 1 - \lambda_l(s)$
Individual phase velocity	$\rho_l \mathbf{u}_l = \mathbf{j}_l + \lambda_l \rho \mathbf{u}; \rho_g \mathbf{u}_g = -\mathbf{j}_l + \lambda_g \rho \mathbf{u}$

$$\mathbf{j}_l = \frac{\lambda_l \lambda_g K \rho}{\mu} \nabla p_c \quad [13]$$

where the definition of various two-phase properties is listed in Table II.²⁹

Methanol transport.—Assuming the vapor-liquid equilibrium of methanol on the anode side and invoking Henry's law, the methanol conservation equation in the anode side can be specifically rewritten as

$$\begin{aligned} & \frac{\partial}{\partial t} \left[c_l^{\text{MeOH}} \left(s + \frac{1-s}{k_H} \right) \right] + \nabla \cdot \left\{ \gamma \mathbf{u} c_l^{\text{MeOH}} \left(s + \frac{1-s}{k_H} \right) \right\} \\ & = \nabla \cdot \left[\left(D_{l,\text{eff}}^{\text{MeOH}} + \frac{D_{g,\text{eff}}^{\text{MeOH}}}{k_H} \right) \nabla c_l^{\text{MeOH}} \right] - \nabla \cdot \left[\left(\frac{1}{\rho_l} \right. \right. \\ & \left. \left. - \frac{1}{k_H \rho_g} \right) c_l^{\text{MeOH}} \mathbf{j}_l \right] + S^{\text{MeOH}} \end{aligned} \quad [14]$$

where

$$S^{\text{MeOH}} = -\frac{j}{6F} - \frac{j_{\text{xover}}}{6F} \quad \text{anode catalyst layer} \quad [15]$$

Assuming complete consumption of crossover methanol at the cathode catalyst layer, and averaging the methanol diffusive flux through the membrane along the catalyst layer thickness, the net methanol crossover flux through the membrane, caused by electro-osmotic drag and diffusion, can be estimated by

$$\frac{j_{\text{xover}}}{6F} = \nabla \cdot \left(n_d^{\text{MeOH}} \frac{i}{F} \right) + \frac{\left(D_m^{\text{MeOH}} c_l^{\text{MeOH}} \right)_{\text{int}}}{\delta_{\text{cata}}} \quad [16]$$

where the methanol electro-osmotic drag coefficient, n_d^{MeOH} , is proportional to the methanol concentration such that

$$n_d^{\text{MeOH}} = n_d^{\text{H}_2\text{O}} \frac{c_l^{\text{MeOH}}}{c_l^{\text{H}_2\text{O}}} \quad [17]$$

and $c_l^{\text{MeOH}}|_{\text{int}}$ denotes the methanol concentration at the interface between the anode catalyst layer and membrane.

Water transport.—Assuming that the water concentration in the gas phase is always saturated and constant at given temperature and pressure, we have that

$$c_g^{\text{H}_2\text{O}} = c_{g,\text{sat}}^{\text{H}_2\text{O}} = \text{const} \quad [18]$$

Then, the water conservation equation in both anode and cathode sides can be derived from Eq. 12 as

$$\frac{\partial c^{\text{H}_2\text{O}}}{\partial t} + \nabla \cdot \{\gamma \mathbf{u} c^{\text{H}_2\text{O}}\} = \nabla \cdot [D_{l,\text{eff}}^{\text{H}_2\text{O}} \nabla c_l^{\text{H}_2\text{O}}] - \nabla \cdot \left[\left(\frac{c_l^{\text{H}_2\text{O}}}{\rho_l} - \frac{c_{g,\text{sat}}^{\text{H}_2\text{O}}}{\rho_g} \right) \mathbf{j}_l \right] + S^{\text{H}_2\text{O}} \quad [19]$$

where the nonzero source term, $S^{\text{H}_2\text{O}}$, only exists in the anode and cathode catalyst layers, given by

$$S^{\text{H}_2\text{O}} = \begin{cases} -\frac{j}{6F}(1 + 6\alpha) & \text{anode catalyst layer} \\ \frac{j}{2F} + \frac{j_{\text{xover}}}{3F} + \alpha \frac{j}{F} & \text{cathode catalyst layer} \end{cases} \quad [20]$$

and the net water flux through the membrane is caused by electro-osmotic drag, diffusion, and hydraulic permeation due to different hydraulic pressures between the anode and cathode, such that

$$\alpha \frac{i}{F} = n_d^{\text{H}_2\text{O}} \frac{i}{F} + N_{m,\text{diff}}^{\text{H}_2\text{O}} - N_{m,\text{pl}}^{\text{H}_2\text{O}} = n_d^{\text{H}_2\text{O}} \frac{i}{F} + \frac{\rho_m D_m^{\text{H}_2\text{O}} \lambda_a^{\text{H}_2\text{O}} - \lambda_c^{\text{H}_2\text{O}}}{EW} - \frac{\rho_l K_m}{M^{\text{H}_2\text{O}} \mu_l \delta_m} \left[\frac{2\sigma_a \cos \theta_a}{r_a} J(s_a) - \frac{2\sigma_c \cos \theta_c}{r_c} J(s_c) \right] \quad [21]$$

where $J(s)$ is Leverett function, given as

$$J(s) = \begin{cases} 1.417(1-s) - 2.120(1-s)^2 + 1.263(1-s)^3 & \theta < 90^\circ \\ 1.417s - 2.120s^2 + 1.263s^3 & \theta > 90^\circ \end{cases} \quad [22]$$

Note that Eq. 21 indicates that the water hydraulic permeation flux is directly proportional to the hydraulic permeability of the membrane, a fundamental parameter requiring experimental measurement, and inversely proportional to the membrane thickness and the pore sizes of anode and cathode backing layers. In practice, the cathode pore size can be engineered to enhance hydraulic permeation by using a highly hydrophobic microporous layer.¹⁻³ Furthermore, the net water transport coefficient through the membrane, α , varies spatially over the membrane.

Oxygen transport.— On the cathode side, oxygen solubility in liquid water is very small and thus, oxygen transport in the liquid phase is neglected in this study. Then, we have that

$$\frac{\partial c^{\text{O}_2}}{\partial t} + \nabla \cdot \{\gamma \mathbf{u} c^{\text{O}_2}\} = \nabla \cdot [D_{g,\text{eff}}^{\text{O}_2} \nabla c_g^{\text{O}_2}] - \nabla \cdot \left[\left(\frac{c_g^{\text{O}_2}}{\rho_g} \right) \mathbf{j}_l \right] + S^{\text{O}_2} \quad [23]$$

where

$$S^{\text{O}_2} = -\frac{j + j_{\text{xover}}}{4F} \quad \text{cathode catalyst layer} \quad [24]$$

Electrochemical kinetics.— Derived from a full system of kinetic equations for the four-step mechanism of methanol oxidation by Meyers and Newman,²⁵⁻²⁷ the anodic transfer current density can be expressed by Tafel approximation of Butler-Volmer equation, such that

$$j = \frac{a_{j_{o,a}}^{\text{ref}} c_l^{\text{MeOH}} \left|_{\text{cata}} \exp\left(\frac{\alpha_a F}{RT} \eta_a\right)}{c_l^{\text{MeOH}} \left|_{\text{cata}} + K_c \exp\left(\frac{\alpha_a F}{RT} \eta_a\right)} \quad [25]$$

where the rate constant, K_c , conveniently controls the transition from the zero-order kinetics of methanol oxidation under high methanol concentration and low overpotential to the first-order kinetics under low methanol concentration and high overpotential. The anode overpotential is defined as

$$\eta_a = \Phi_s - \Phi_e - U_a^o \quad [26]$$

Similarly, the cathodic transfer current density can be written as

$$j_c = a_{j_{o,c}}^{\text{ref}} \left(\frac{c_g^{\text{O}_2} \left|_{\text{cata}}}{c_g^{\text{O}_2,\text{ref}} \right.} \right) (1-s) \exp\left(-\frac{\alpha_c F}{RT} \eta_c\right) \quad [27]$$

where

$$j_c = j + j_{\text{xover}} \quad [28]$$

and the term $(1-s)$ accounts for the fraction of catalytic surfaces rendered inactive by the presence of liquid water in the cathode catalyst layer, and cathode overpotential is

$$\eta_c = \Phi_s - \Phi_e - U_c^o \quad [29]$$

Under the assumption of a perfectly conductive electronic phase of anode and cathode catalyst layers, the electronic phase potential, Φ_s , becomes zero for the anode and is equal to the cell voltage for the cathode.

The electrolyte phase potential, Φ_e , is given by the proton transport equation

$$0 = \nabla \cdot (\kappa_{\text{eff}} \nabla \Phi_e) + S_\Phi \quad [30]$$

where

$$S_\Phi = \begin{cases} j & \text{anode catalyst layer} \\ -j_c + j_{\text{xover}} & \text{cathode catalyst layer} \end{cases} \quad [31]$$

Equation 31 indicates that protons are generated in the anode catalyst layer and consumed in the cathode catalyst layer. The proton conductivity of the membrane, κ_{eff} , is assumed constant in this work because the membrane is well hydrated in a liquid-feed DMFC.

Phase saturations.— Liquid saturation is a key parameter in the two-phase flow model. Here, we obtain the liquid saturation from the mixture water molar concentration via

$$s = \frac{c^{\text{H}_2\text{O}} - c_{g,\text{sat}}^{\text{H}_2\text{O}}}{c_l^{\text{H}_2\text{O}} - c_{g,\text{sat}}^{\text{H}_2\text{O}}} \quad [32]$$

where $c_l^{\text{H}_2\text{O}}$ is simply calculated by

$$c_l^{\text{H}_2\text{O}} = \frac{\rho_l}{M^{\text{H}_2\text{O}}} \quad [33]$$

Boundary conditions.— All governing equations of the 3D model are summarized in Table I, with eight unknowns: \mathbf{u} (three components), p , c_l^{MeOH} , c^{O_2} , $c^{\text{H}_2\text{O}}$, and Φ_e . Their corresponding boundary conditions are described as follows:

Flow inlet boundaries.— The inlet velocity \mathbf{u}_{in} in a flow channel is expressed by the respective stoichiometric flow ratio, i.e., ξ_a or ξ_c , defined at a reference current density, i^{ref} , as

$$\xi_a = \frac{c_l^{\text{MeOH}} \mathbf{u}_{\text{in},a} A_{\text{cross},a}}{i_{\text{ref}} A} \quad \text{and} \quad \xi_c = \frac{c^{\text{O}_2} \mathbf{u}_{\text{in},c} A_{\text{cross},c}}{i_{\text{ref}} A} \quad [34]$$

where $A_{\text{cross},a}$ and $A_{\text{cross},c}$ are the flow cross-sectional areas of the anode and cathode flow channels, respectively. The anode inlet methanol concentration is given as an operating parameter and the cathode oxygen molar concentration determined by the cathode inlet pressure, temperature, and relative humidity according to the ideal gas law.

Outlet boundaries.— Fully developed or no-flux conditions are applied

$$\frac{\partial \mathbf{u}}{\partial n} = 0 \quad \frac{\partial p}{\partial n} = 0 \quad \frac{\partial c^k}{\partial n} = 0 \quad \text{and} \quad \frac{\partial \Phi_e}{\partial n} = 0 \quad [35]$$

Walls.— No-slip and impermeable velocity and no-flux conditions are applied

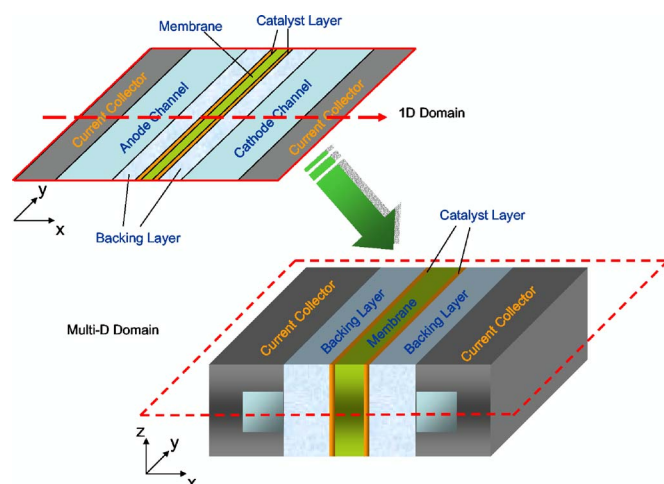


Figure 1. (Color online) Simulation domains for 1D and 3D models.

$$\mathbf{u} = 0, \quad \frac{\partial p}{\partial n} = 0 \quad \frac{\partial c^k}{\partial n} = 0 \quad \text{and} \quad \frac{\partial \Phi_e}{\partial n} = 0 \quad [36]$$

Model summary.— The present model can address species transport occurring in a DMFC in three dimensions and in all the components of flow channels, backing, catalyst layers, and the membrane, as shown in Fig. 1. For instance, the model can address reactant depletion along the flow channel as well as land effects causing mass transport limiting currents along the in-plane direction from a channel to a land.

Numerical procedures.— Besides intricate couplings between species transport equations, a numerically complicated problem for 3D modeling of DMFC is the strong coupling between the species transport equations and electrochemical kinetics that are dependent on species concentrations. Another computational challenge is the need for large meshes for 3D geometries with an aspect ratio of the order of 100. Therefore, the model must seek a stable and efficient solution procedure.

Numerical strategies.— The 3D, two-phase DMFC model was implemented into commercial software, Fluent, through user-defined functions, or UDFs, provided by Fluent in DEFINE macros, which are employed to implement sources terms, diffusion coefficients, material properties, and boundary conditions. Because incompressible and low Reynolds number flows are solved in the present 3D model, a segregated numerical solver based on semi-implicit method of pressure linked-equation (SIMPLE) method was employed to take full advantage of its efficiency and robustness. The species equations of methanol, water, and oxygen, as well as the proton transport equation, were implemented using user-defined scalars (UDS). A first-order upwind scheme was applied to discretize the convection terms in all the conservation equations, including momentum and species equations, because of large grid stretch ratios and significant differences of mesh sizes arising from geometric size differences in different layers and orientations of a DMFC.

In the present 3D model based on the molar concentration, conservation equations of mass and momentum, representing the flow field, were decoupled from those of species concentrations and the electrolyte potential; these latter equations can, therefore, be solved separately. The mass and momentum equations were first solved to find a converged flow field, followed by solution of the species and charge equations with the mass and momentum equations turned off. By taking advantage of this decoupling in the molar-concentration formulation, more than 30% computational time was saved as compared to solving all conservation equations simultaneously. As convergence criteria, we set the residuals for all governing equations at

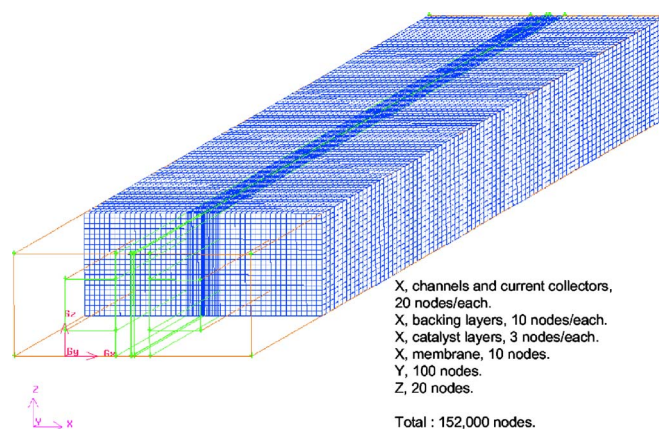


Figure 2. (Color online) Numerical mesh used for 3D simulations.

less than 10^{-6} . Each 3D calculation took 4–6 h CPU time on a Pentium IV 2.4 GHz desktop computer with 1 GB memory.

Numerical mesh.— To solve the 3D model in Fluent, a numerical mesh was needed and could be generated in GAMBIT software based on dimensions and computational ability. As shown in Fig. 2, there is a total of 152,000 grid points in the mesh. This mesh has been tested to be sufficient by a careful grid-independence study.

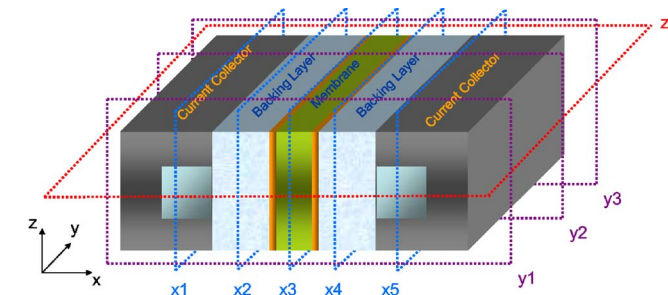
Results and Discussion

The 1D version of the present DMFC model has been validated against experimental data of methanol crossover, water crossover, and polarization curves.³¹ Good agreement was achieved, demonstrating the validity of the present physical model. In the following, focus is placed on elucidating 3D simulation results for a geometry described in Table III. The cell is operated at 60°C, with 2 M methanol solution at the anode inlet and 1 atm fully humidified air at the cathode inlet, respectively. The stoichiometric flow ratios in the anode and cathode flow channels are set to be 2 and 3, respectively. To clearly understand numerical results shown in this section, several representative planes in the 3D domain are described in Fig. 3 for presentation of numerical results.

Methanol concentration.— Methanol concentration contours predicted by the model on various planes are shown in Fig. 4-6. Along the flow direction, the methanol concentration in the anode channel is dominated by convection while it is mainly determined

Table III. 3D cell geometry and operating conditions.

Cell length	0.1 m
Cell width	2×10^{-3} m
Anode channel width	1×10^{-3} m
Anode backing thickness	300×10^{-6} m
Anode catalyst thickness	10×10^{-6} m
Membrane thickness	50×10^{-6} m
Cathode catalyst thickness	10×10^{-6} m
Cathode backing thickness	300×10^{-6} m
Cathode channel width	1×10^{-3} m
Operating temperature	60°C
Anode channel pressure	1 atm
Cathode channel pressure	1 atm
Flow stoichiometry of anode channel	2
Flow stoichiometry of cathode channel	3
Inlet methanol concentration at anode	2000 mol/m ³ (2M)
Inlet liquid saturation at anode	100%
Inlet liquid saturation at cathode	0% (fully humidified air)
Interfacial liquid saturation at the cathode backing layer	0%
Cell operating voltage	0.4 V



Plane	Location
X1	1/2 of anode channel thickness
X2	1/2 of anode backing thickness
X3	1/2 of membrane thickness
X4	1/2 of cathode backing thickness
X5	1/2 of cathode channel thickness
Y1	1/10 of cell length
Y2	1/2 of cell length
Y3	9/10 of cell length
Z	1/2 of cell width

Figure 3. (Color online) Illustration of several planes in the 3D domain for presentation of 3D model simulation results.

by diffusion in the anode backing layer. In Fig. 4b, it is evident that methanol concentration in the backing is higher under the flow channel than under the lands, demonstrating the land effect in limiting methanol transport in the anode. Also, the gradient of methanol concentration in the channel cross section increases from the inlet to the outlet (i.e., from plane Y1 to Y2 to Y3). Although the average methanol concentration in the liquid exiting from the channel is still high, about 1.2 M (see Fig. 4a), the concentration inside the catalyst layer is very low near the exit, about 0.1 M, due to the insufficient methanol transport under the lands of the anode. Similar methanol concentration contours can also be seen in Fig. 6 on plane Z, in the middle of the cell width. It is shown that, even with excess methanol fed into the anode channel, the electrochemical reaction in the anode

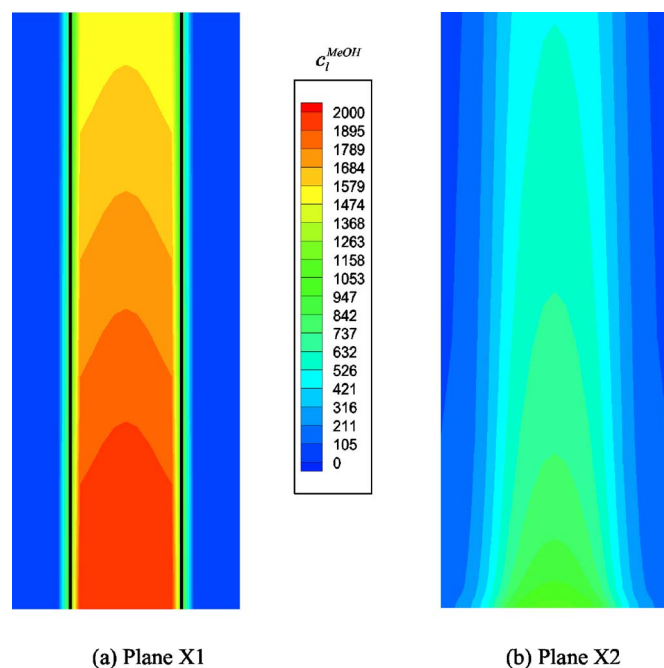


Figure 4. (Color online) Methanol concentration (mol/m^3) distribution in (a) the anode channel and (b) backing layer.

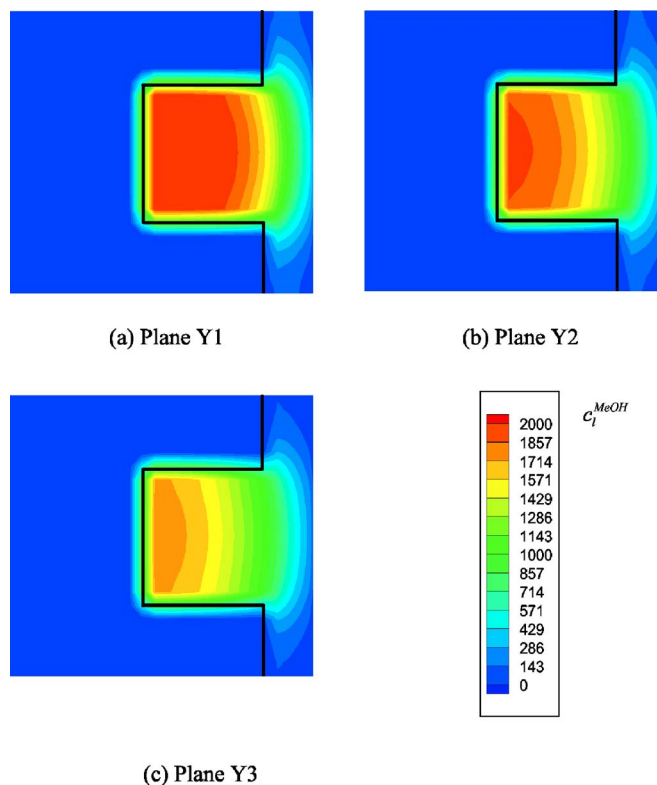


Figure 5. (Color online) Methanol concentration (mol/m^3) distributions near (a) the inlet, (b) middle of the cell length, and (c) near the outlet, in the anode.

catalyst layer is restricted by the methanol transport limitation. This methanol transport limiting phenomenon can only be captured by a 3D model.

Oxygen concentration.— On the cathode side, oxygen concentration distributions are presented in Fig. 7 and 8. Similar to the methanol concentration on the anode side, the oxygen concentration shows a larger gradient in the backing layer than in the cathode channel. Although the oxygen concentration is also affected by lands in the cathode bipolar plate, the effect is not as strong as that for methanol transport, due largely to the much larger gas diffusivity of O_2 . In addition, oxygen concentration shows smaller gradients in both the cathode channel and backing layer than those of the methanol concentration. The largest variation in the oxygen concentration is no greater than 20% of the inlet oxygen concentration, while the methanol concentration is almost completely depleted in the land areas of the anode catalyst layer. The comparison between the methanol and oxygen concentration distribution clearly indicates that the land and flow field design on the anode side is more important in affecting the limiting current density of a DMFC.

Liquid saturation.— Critical to the understanding of water transport in a DMFC, the liquid saturation contours on several planes are shown in Fig. 9-11. Overall, it is seen that the liquid saturation profile in the anode side is quite different from that of the cathode side. This is due to the different inlet conditions as well as two-phase transport properties in the different range of liquid saturation. Note that the anode is liquid dominated, whereas the cathode is gas dominated.

Along the anode channel, the liquid saturation shows about 7% change from 100% at the inlet to 93% at the outlet, while the saturation change is about 10% in the anode backing layer. This means that the two-phase flow pattern and species transport in the anode channel approaches the pure liquid flow limit and evolves into the bubbly flow with a small gas fraction. In the anode backing layer,

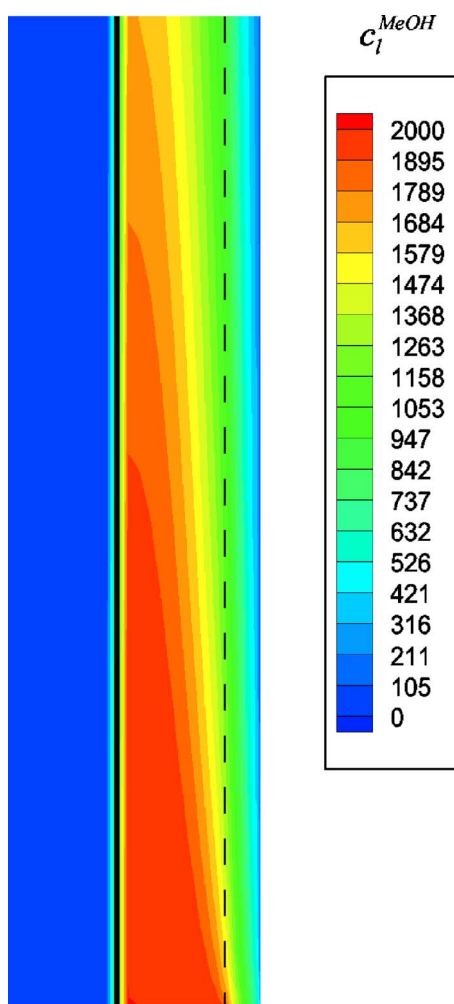


Figure 6. (Color online) Methanol concentration (mol/m^3) distribution in the middle of cell width (plane Z).

the liquid saturation under the channel is higher than under the land due to more efficient removal of CO_2 gas. However, unlike the trend in methanol and oxygen concentrations, the liquid saturation under the land is slightly lower near the inlet than near the outlet, shown in Fig. 9b. This is because, with the higher current density generated near the inlet, water transport by electro-osmotic drag from the anode to cathode is much larger than hydraulic permeation from the cathode to anode. With the decreasing methanol concentration in the anode catalyst layer along the flow direction, however, the local current density near the outlet decreases, and thus weakens the water electro-osmotic drag from the anode to cathode. Therefore, with water hydraulic permeation from the cathode to anode dominating the electro-osmotic flux, the liquid saturation in the anode becomes higher near the outlet under the land. Along the flow direction, the liquid saturation in the channel shows a larger gradient near the outlet than near the inlet, as seen in Fig. 10.

The liquid saturation in the cathode is quite different from the anode. As shown in Fig. 11, the liquid saturation distribution in the cathode backing layer is greatly affected by the land. The liquid saturation in the channel area of the backing layer is lower than that under the land. With water generation in the cathode catalyst layer and water transport from the anode to cathode, the highest liquid saturation is about 7% in the cathode backing layer under given operating conditions. The small gradient of liquid saturation is due to the relatively large capillary diffusivity at liquid saturation below 10%.

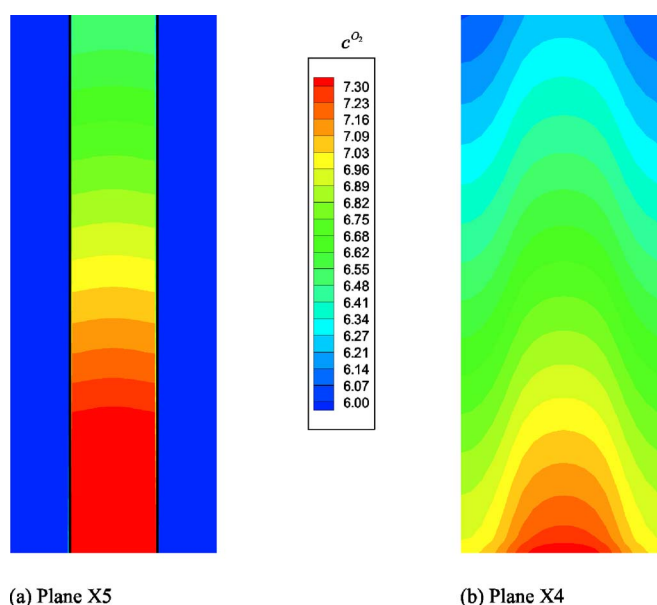


Figure 7. (Color online) Oxygen concentration (mol/m^3) distributions in (a) cathode channel and (b) backing layer.

Current density and crossover current density.— Among the most desirable outputs from the 3D DMFC model are the current density distribution, the crossover current density distribution, and the inter-relationship between them. The current density distribution in a DMFC has been measured by Mench and Wang,³² but the measurement of methanol crossover current density distribution has yet to be reported. This information, however, can be made available from the present 3D model. The predicted current density and crossover current distributions in the middle of the membrane at the cell voltage of 0.4 V are shown in Fig. 12. Under the given conditions,

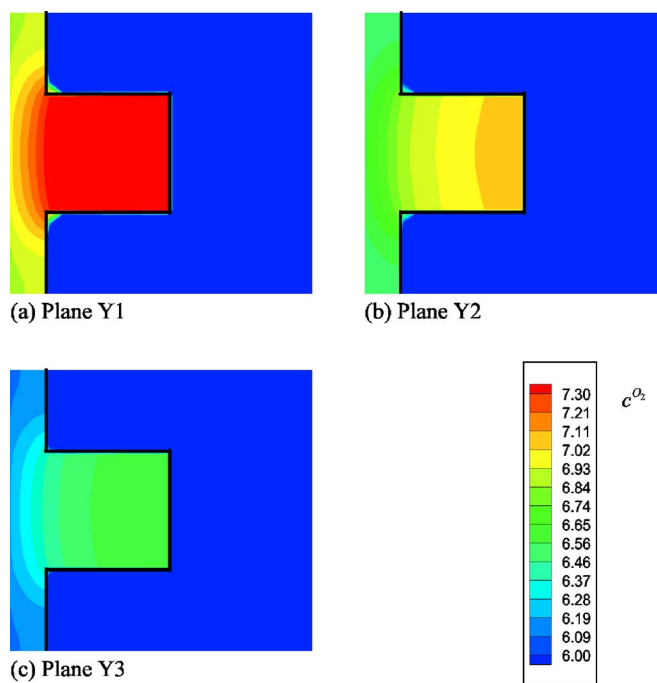


Figure 8. (Color online) Oxygen concentration (mol/m^3) distributions near (a) the inlet, (b) middle of the cell length, and (c) near the outlet, in the cathode.

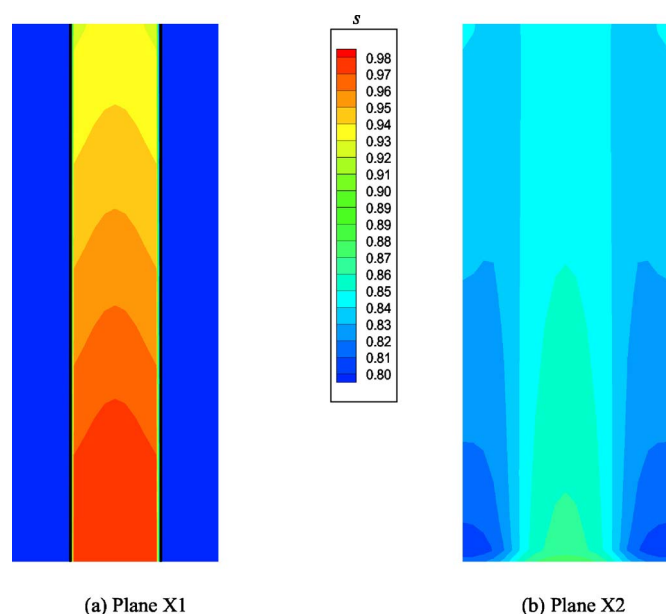


Figure 9. (Color online) Liquid saturation distributions in the (a) anode channel and (b) backing layer.

the current density is relatively uniform in the channel region of the membrane, but varies greatly in the land areas of the membrane, due primarily to the severe methanol transport limitation there. Moreover, the highest local current density does not occur at the inlet, although the highest methanol concentration is there. This can be explained by methanol crossover. Near the inlet, methanol crossover is most severe due to both methanol diffusion driven by the highest methanol concentration and electro-osmotic drag under the relatively high current density, as can be seen from Fig. 12b. The large methanol crossover current leads to a severe mixed potential caused by the parasitic methanol oxidation reaction (MOR) at the cathode

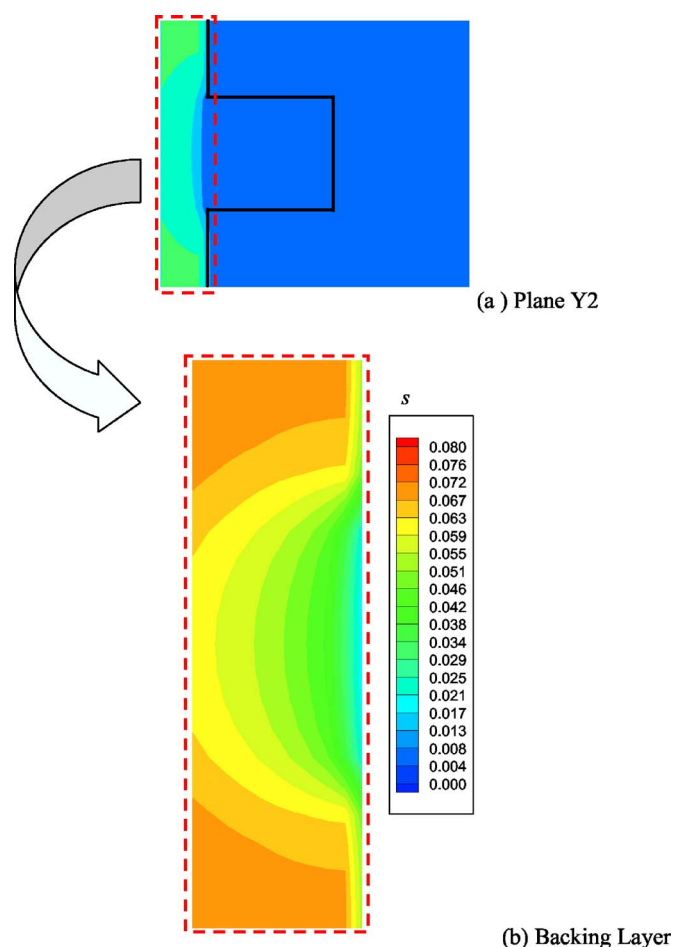


Figure 11. (Color online) Liquid saturation in (a) cathode side and (b) in the cathode backing layer.

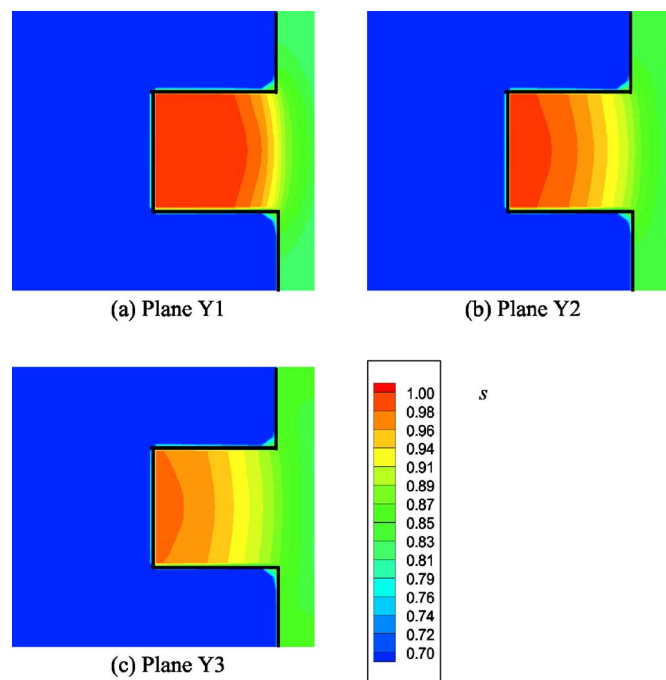


Figure 10. (Color online) Liquid saturation distributions near (a) the inlet, (b) middle of the cell length, and (c) near the out, in the anode.

catalyst layer, thus reducing the operating current density of the cell. With decreasing methanol concentration along the flow direction, methanol crossover decreases quickly, from 0.30 A/cm² at the inlet to about 0.15 A/cm² in the middle of the flow direction. Therefore,

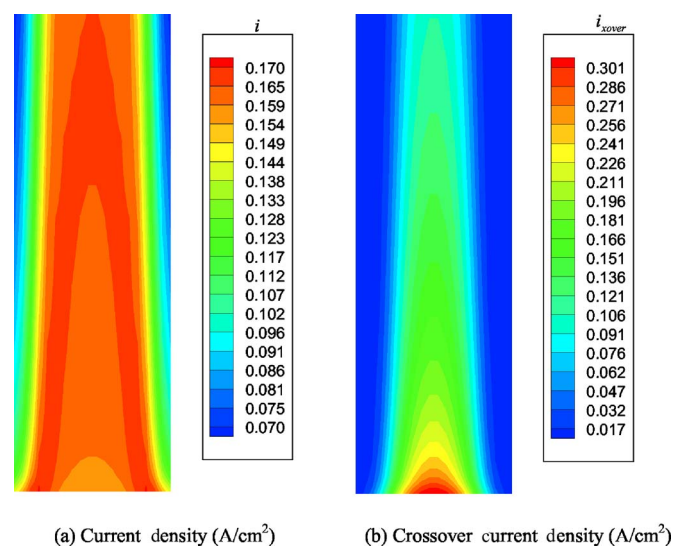


Figure 12. (a) Current density and (b) crossover current density distributions in the middle of the membrane (plane X3) at cell voltage of 0.4 V.

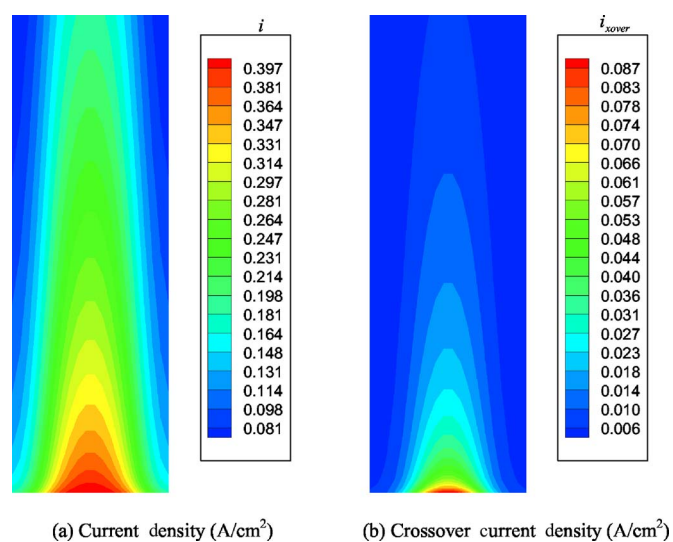


Figure 13. (a) Current density and (b) crossover current density distribution in the middle of the membrane (plane X3) at cell voltage of 0.2 V.

the highest local current density occurs in the middle section of the flow due to a combination of weak methanol crossover, still relatively high methanol concentration, and zero-order kinetics of the anode reaction.

In the land areas of the membrane, the current density distribution is controlled by the local methanol concentration because, due to insufficient methanol transport, the MOR is already a first-order reaction under small methanol concentrations there. Under the given operating conditions, the lowest current density under the lands of the current collector is only about 60% of that in the channel area of the membrane. Therefore, the geometry of lands and flow field appears to be important for uniform current distribution and high cell performance. More detailed discussion on the land effect related to electron transport in a portable DMFC can be found in Liu.³¹

In comparison to the 0.4 V case, the current density and crossover current density distributions at 0.2 V are shown in Fig. 13. It is evident that the current distribution at 0.2 V is completely controlled by the methanol concentration distribution in the anode catalyst layer due to the larger methanol consumption rate; thus, methanol crossover is too weak to affect the current density distribution. The highest crossover current density at the cell voltage of 0.2 V is only 27% of that at 0.4 V.

Based on the current density and methanol crossover current density results, it can be said that the anode flow field design and the feeding methanol concentration are two critical parameters for overall cell performance of a portable DMFC. If methanol concentrations in the anode channel can be more uniform along the flow direction, for example, by a face-feeding strategy, a more uniform current density distribution and thus a better cell performance may result.

Conclusions

In this paper, a three-dimensional, two-phase model was developed, considering methanol, water, and oxygen transport processes as well as electrochemical phenomena in all components of a portable DMFC. Conservation equations of mass, momentum, species transport, and proton transport with electrochemical reactions were numerically solved using commercial software, Fluent, with the capability of simulating realistic single cells using large mesh. The numerical results not only revealed information such as the methanol transport limitation due to the land effect and nonuniform current density distribution affected by spatially distributed methanol crossover rate, but also suggested a key parameter, the anode flow field geometry, to achieve optimized cell performance.

Acknowledgments

Support for this work by ECEC industrial sponsors is gratefully acknowledged.

The Pennsylvania State University assisted in meeting the publication costs of this article.

List of Symbols

a_{j_0}	total exchange current density, A/m ³
A	reaction area, m ²
c	molar concentration, mol/m ³
D	diffusivity, m ² /s
EW	equivalent weight of the membrane, kg/mol
F	Faraday's constant, 96,485 C/mol
i	operating current density, A/m ²
j	volumetric current density, A/m ³
k_H	Henry's law constant
k_r	relative permeability
K	permeability of porous medium, m ²
K_c	reaction constant
\dot{m}	mass source term in governing equations
M	molecular weight, kg/mol
n_d	electro-osmotic drag coefficient
p	pressure, Pa
p_c	capillary pressure, Pa
r	radius of porous medium pores, m
s	liquid water saturation
S^k	molar source term of k species
\mathbf{u}	velocity, m/s
V_{cell}	cell voltage, V
U^0	standard equilibrium potential, V
Y	mass fraction, kg/kg
Greek	
α	net water transport coefficient through the membrane
α_i	current transfer coefficient at anode or cathode ($i = a$ or c)
δ	thickness, m
ϵ	porosity of porous medium
Φ	phase potential, V
γ	advection correction factor
η_i	overpotential of anode or cathode ($i = a$ or c), V
κ	ionic conductivity of membrane, S/m
$\lambda^{\text{H}_2\text{O}}$	water content in the membrane
λ_i	relative mobility of i phase ($i = l$ or g)
μ	viscosity, kg/(m s)
ν	kinetic viscosity, m ² /s
θ	contact angle, °
ρ	density, kg/m ³
σ	surface tension, N/m
ξ	stoichiometric flow ratio
Subscripts	
a	anode
c	cathode
cata	catalyst layer
cross	cross section
diff	diffusion
e	electrolyte
eff	effective
g	gas phase
in	inlet
int	interface
l	liquid phase
m	membrane
pl	hydraulic permeation
s	solid or electronic phase
sat	saturated
xover	crossover
Superscripts	
CO ₂	carbon dioxide
H ₂ O	water
MeOH	methanol
O ₂	oxygen
k	species
ref	reference

References

1. C. Y. Wang, *Chem. Rev. (Washington, D.C.)*, **104**, 4727 (2004).
2. G. Q. Lu, F. Q. Liu, and C. Y. Wang, *Electrochem. Solid-State Lett.*, **8**, A1 (2005).
3. F. Q. Liu, G. Q. Lu, and C. Y. Wang, *J. Electrochem. Soc.*, **153**, A543 (2006).
4. G. T. Burstein, C. J. Barnett, A. R. Kucernak, and K. R. Williams, *Catal. Today*, **38**, 425 (1997).
5. S. Wasmus and A. Kuver, *J. Electroanal. Chem.*, **461**, 14 (1999).
6. A. Hamnett, *Catal. Today*, **38**, 445 (1997).
7. H. N. Dinh, X. Ren, F. H. Garzon, P. Zelenay, and S. Gottesfeld, *J. Electroanal. Chem.*, **491**, 222 (2000).
8. L. Liu, C. Pu, R. Viswanathan, Q. Fan, R. Liu, and E. S. Smotkin, *Electrochim. Acta*, **43**, 3657 (1998).
9. A. S. Arico, P. Creti, E. Modica, G. Monforte, V. Baglio, and V. Antonucci, *Electrochim. Acta*, **45**, 4319 (2000).
10. D. Chu and R. Jiang, *Solid State Ionics*, **148**, 591 (2002).
11. S. R. Narayanan, H. Frank, B. Jeffries-Nakamura, M. Smart, W. Chun, G. Halpert, J. Kosek, and C. Cropley, in *Proton Conducting Membrane Fuel Cells I*, S. Gottesfeld, G. Halpert, and A. R. Landgrebe, Editors, PV 95-23, p. 278, The Electrochemical Society Proceedings Series, Pennington, NJ (1995).
12. X. Ren, T. A. Zawodzinski, Jr., F. Uribe, H. Dai, and S. Gottesfeld, in *Proton Conducting Membrane Fuel Cells I*, S. Gottesfeld, G. Halpert, and A. R. Landgrebe, Editors, PV 95-23, p. 278, The Electrochemical Society Proceedings Series, Pennington, NJ (1995).
13. J.-T. Wang, S. Wasmus, and R. F. Savinell, *J. Electrochem. Soc.*, **143**, 1233 (1996).
14. S. Hikita, K. Yamane, and Y. Nakajima, *JSAE Review*, **22**, 151 (2001).
15. S. C. Kelly, G. A. Deluga, and W. H. Smyrl, *Electrochem. Solid-State Lett.*, **3**, 407 (2000).
16. G. Q. Lu, C. Y. Wang, T. J. Yen, and X. Zhang, *Electrochim. Acta*, **49**, 821 (2004).
17. P. Argyropoulos, K. Scott, and W. M. Taama, *J. Appl. Electrochem.*, **29**, 661 (1999).
18. G. Lu and C. Y. Wang, *J. Power Sources*, **134**, 33 (2004).
19. J. Wang and R. F. Savinell, in *Electrode Materials and Processes for Energy Conversion and Storage*, S. Srinivasan, D. D. Macdonald, and A. C. Khandkar, Editors, PV 94-23, p. 326, The Electrochemical Society Proceedings Series, Pennington, NJ (1994).
20. S. F. Baxter, V. S. Battaglia, and R. E. White, *J. Electrochem. Soc.*, **146**, 437 (1999).
21. A. A. Kulikovskiy, J. Divisek, and A. A. Kornyshev, *J. Electrochem. Soc.*, **147**, 953 (2000).
22. A. A. Kulikovskiy, *J. Appl. Electrochem.*, **30**, 1005 (2000).
23. K. Scott, P. Argyropoulos, and K. Sundmacher, *J. Electroanal. Chem.*, **477**, 97 (1999).
24. P. Argyropoulos, K. Scott, and W. M. Taama, *J. Appl. Electrochem.*, **30**, 899 (2000).
25. J. P. Meyers and J. Newman, *J. Electrochem. Soc.*, **149**, A710 (2002).
26. J. P. Meyers and J. Newman, *J. Electrochem. Soc.*, **149**, A718 (2002).
27. J. P. Meyers and J. Newman, *J. Electrochem. Soc.*, **149**, A729 (2002).
28. Z. H. Wang, C. Y. Wang, and K. S. Chen, *J. Power Sources*, **94**, 40 (2001).
29. C. Y. Wang and P. Cheng, *Adv. Heat Transfer*, **30**, 93 (1997).
30. Z. H. Wang and C. Y. Wang, *J. Electrochem. Soc.*, **150**, A508 (2003).
31. W. Liu, Ph.D. Thesis, The Pennsylvania State University, University Park, PA (2005).
32. M. M. Mench and C. Y. Wang, *J. Electrochem. Soc.*, **150**, A79 (2003).